Evaluation of the effects of bismuth oxide (Bi₂O₃) micro and nanoparticles on the mechanical, microstructural and γ-ray / neutron shielding properties of Portland cement pastes

Pawel Sikora[1,2,*], Ahmed M. El-Khayatt[3,4], H.A. Saudi[5], Sang-Yeop Chung[6], Dietmar Stephan[1], Mohamed Abd Elrahman[7,†]

[1] Building Materials and Construction Chemistry, Technische Universität Berlin, Germany
[2] Faculty of Civil and Environmental Engineering, West Pomeranian University of Technology Szczecin, Szczecin
[3] Department of Physics, College of Science, Imam Mohammad Ibn Saud Islamic University, (IMSIU), Riyadh, Saudi Arabia
[4] Reactor Physics Department, Nuclear Research Centre, Atomic Energy Authority, 13759, Cairo, Egypt
[5] Department of Physics, Faculty of Science, Al-Azhar University, Women Branch, Nasr City, Cairo, Egypt
[6] Department of Civil and Environmental Engineering, Sejong University, Seoul 05006, Republic of Korea
[7] Structural Engineering Department, Mansoura University, Mansoura City 35516, Egypt

Abstract

This study presents a comparison of the effects of micro-Bi_2O_3 and nano-Bi_2O_3 powders on the mechanical, microstructural and gamma / neutron shielding properties of Portland cement pastes. Cement pastes with various ratios of cement (up to 30 wt.-%) replaced with Bi_2O_3 micro and nanoparticles were prepared. Consistency, compressive strength, water accessible porosity and mercury intrusion porosimetry tests were performed, in order to characterize their engineering properties. In addition, experimental and theoretical evaluations of γ-ray and neutron shielding properties were performed. The results showed that the incorporation of Bi_2O_3 powders gradually leads to a decline in cement pastes' compressive strength and an increase in their porosity, as the amount of powder is increased. However, the deterioration rate varies depending of type of powder used, in favor of nano-Bi_2O_3. Gamma attenuation tests results indicate that the addition of Bi_2O_3 powders enhances the shielding capability of pastes, in the energy range of interest (0.08-2.614 MeV). However, the effects of particle size on γ-ray attenuation are negligible in that energy range. Slow neutron attenuation study showed that the addition of nano-Bi_2O_3 improved the shielding ability of cement pastes, with enhancements ranging between 15.3 % and 25.5 % for samples with 5 and 30 wt.-% nano-Bi_2O_3, respectively. In conclusion, this study shows that the addition of nano or micro-Bi_2O_3 is effective in producing lead-free cementitious composites with improved γ-ray and neutron shielding properties. Unlike gamma shielding, nano-sized Bi_2O_3 has a better ability to attenuate neutrons, in comparison to their micro-sized counterparts.

Corresponding authors: (1) Pawel Sikora – email: pawel.sikora@zut.edu.pl; Building Materials and Construction Chemistry, Technische Universität Berlin, Germany and (2) Mohamed Abd Elrahman – email: mohamedattia@mans.edu.eg; Structural Engineering Department, Mansoura University, Mansoura City 35516, Egypt.

1. Introduction

Humans have long recognized the benefits of ionizing radiation, as well as the risks of exposure to it, especially in medical applications, where X-rays and high-energy gamma rays have been used in radiation therapy to control and treat cancerous tumors [1]. Conventional building materials, such as concrete blocks [2] and bricks [3], can be used for a protection purpose from ionizing radiation. Materials with high atomic number (High-Z) can be used to manufacture conventional blocks and multi-leaf collimators (MLCs) to form better beams and to reduce the absorbed dose in normal tissue. To date, lead (Pb) is the most commonly used material, due to its high atomic number (Z), low cost and abundance [4-6]. Interest in lead-free radiation shields has increased in recent years, since a great deal of concern has been voiced regarding the potential toxicity of lead and its compounds, both to humans and the environment as well as high costs for dismantling and disposal [7].

Concrete is one of the most common materials used for radiation protection in radiation therapy facilities and nuclear reactors, as well as for preventing radiation leakage from radioactive sources. Since one of the main concrete components is aggregate, radiation shielding properties of concrete can be controlled by choice of proper normal- or heavy-weight [8-10] aggregate type. It is an inexpensive material with a high potential for incorporating a great variety of wastes and secondary raw materials [11-13]. In this regard, extensive research is being conducted in order to replace potentially harmful lead-incorporated cementitious composites with environmentally friendly metal oxides such as Bi_2O_3 [14-16], Fe_2O_3/Fe_3O_4 [17-19] or TiO_2 [20]. Bismuth is a higher Z metal than lead with a lower density. It ultimately produces less secondary radiation. Many investigations related to the introduction of micro and nano-sized Bi_2O_3 powders, as environmentally friendly radiopacifiers in the field of polymer [21-22], glass systems [23-26] as well as dental cement [27-29] technology have been conducted.

In contrast, limited knowledge related to the incorporation of Bi_2O_3 powders as potential radiation shielding additives in cement-based composites for construction, is available. As far as the authors are aware, only a few publications related to this field are available. However, most of this research has focused on aspects of gamma-ray attenuation capabilities, with no neutron shielding evaluations being available. For instance, Azimkhani et al. [30] have evaluated the effects of 5, 10 and 15 wt.-% replacement of cement in normal-weight and heavy-weight concrete, showing that the incorporation of Bi_2O_3 powder has a beneficial effect on the gamma-ray shielding of concrete specimens at 662 keV. In addition, the incorporation of 5 and 10 wt.-% Bi_2O_3 powder results in slight compressive strength improvements in concretes, though higher concentrations result in negligible effect on strength. In works [31] and [32], the authors evaluated the effects of low dosages of nano-Bi_2O_3 (2, 4 and 6 wt.-%) as a cement replacement, on the properties of heavy-weight concrete mixes. Improvements in gamma-ray radiation shielding, at energy levels of 662, 1173 and 1332 keV, were demonstrated, both in ambient as well as in elevated temperature conditions (up to 600 °C). In addition, a slight compressive strength improvement in their concrete samples was reported. Yao et al. [33] have evaluated the effects of the addition of Bi_2O_3 powder to cement, in the amount of 5, 10, 15, 20 and 25 wt.-%, on the shielding and compressive strength of concretes. Their experimental results showed that higher compressive strengths and higher linear attenuation coefficients are observed in concrete mixtures, in which cement is replaced with Bi_2O_3 nanoparticles.

Furthermore, the superior performance of concrete mixtures containing nano and micro Bi_2O_3 particles, has also been studied theoretically by Tekin et al. [34] and Verdipoor et al. [35], using the Monte Carlo (MC) method. Their results confirm that nano-sized particles have superior effects on the gamma-ray shielding ability of concrete in the photon energy ranges, 0.142–1.33 MeV and 0.356-1.33 MeV, respectively.

At this point, it is important to mention that the basic assumption of the shielding superiority of nano-sized particles, over their micro-sized counterparts, is that the use of the former leads to a large surface-area-to-volume ratio, thus resulting in a higher radiation absorption. This is because nano-sized particles produce a more uniform distribution, higher particle density and a lower grain size inside the matrix, compared to microparticles. However, in many experimental studies this assumption has not been observed; i.e. higher attenuation properties, resulting from the grain size effect, have not been seen in the case of energies greater than 30 keV, but only at low energies (i.e., < 30keV) [36-40]. Consequently, differences between composites containing nanoparticles and those containing microparticles, actually become insignificant at higher energies. Furthermore, Shik and Gholamzadeh [41] have found that Poly(vinyl chloride) composite emulsion composites containing PbO microparticles can better attenuate photons with higher energies. However, all the above-mentioned studies were carried out with respect to diagnostic X-rays and they are characterized by a lack of experimental data related to higher energies. Furthermore, there are also differences between the results of these studies and theoretical calculations reported elsewhere [34,35]. This has prompted us to carry out further experimental investigations, evaluating the effects of Bi_2O_3 particle size on radiation shielding at higher energies.

Based on the literature review above, it can be concluded that the state-of-the-art regarding the effects of Bi_2O_3 powders is limited, especially in regard to nano-sized admixtures and their shielding properties against γ and neutron radiation. This necessitates more research, in order to fully understand the effects of Bi_2O_3 nanoparticle content and size on the structural, physical, mechanical and radiation shielding properties of concrete. Nano-sized particles exhibit spectacular chemical and physical properties, when compared to their corresponding micro-sized materials as such, when added to cementitious composites, nanomaterials can effectively fill the voids in the cement matrix, acting as nucleating agents as well as exhibiting significant

pozzolanic activity [42,43]. In addition, nanoparticles seems to be viable solution that can be incorporated as additives to cement-based composites and this is due the production costs of nanoparticles which has been significantly decreased over years with commercially available products dedicated for construction industry [44,45].

This study aims to comprehensively evaluate, both experimentally and theoretically, the effects of nano-Bi_2O_3 and micro-Bi_2O_3 powders on the gamma-ray, fast, slow, as well as thermal neutrons on shielding properties of Portland cement composite pastes. In addition, the study investigates the mechanical and microstructural properties of cement pastes, for comparison and to provide insight into the effects of different sized Bi_2O_3 particles, on the performance of cementitious composites. As an outcome, a lead-free Portland cement-based shielding material is proposed.

2. Materials and Methods
2.1. Materials

CEM I 42.5 R Portland cement (conforming to EN 197-1) and tap water (conforming to EN 1008) were used to produce the cement pastes. The chemical composition of the cement is presented in Table 1.

Table 1. Chemical compositions of Portland cement [wt.-%]

Material	CaO	SiO_2	Al_2O_3	Fe_2O_3	MgO	Na_2O	K_2O	Loss on ignition	Specific Density (g/cm^3)
CEM I 42.5 R	64.2	18.8	5.1	3.3	1.8	0.1	0.9	3.05	3.11

Two types of bismuth (III) oxide particles were used: Bi_2O_3 microparticles obtained from Keten, Poland and Bi_2O_3 nanoparticles obtained from Sigma-Aldrich, Poland. Scanning electron microscope (SEM) micrographs of the micro and nanoparticles are presented in Figure 1. Clear difference in the morphology of the powders can be distinguished. Primary Bi_2O_3 nanoparticles exhibts more spherical and regular shape, while microparticles are more irregular with higher size of primary particles when compared to nano-Bi_2O_3. According to producer data the size of primary particle of Bi_2O_3 nanoparticles is ranging between 90-210 nm which was confirmed by our SEM study. Thermogravimetric analysis (Figure 2), performed with the use of a G 209 Tarsus F3 (Netzsch) instrument (under a nitrogen atmosphere), confirmed the high thermal stability of Bi_2O_3 nanoparticles up to 800 °C [46], while in the case of Bi_2O_3 microparticles, a small loss over the entire temperature range was reported. As reported by Zhu et al. [47] this can be attributed to moisture absorption and combined water.

Figure 3 presents the particle size distribution (PSD) of powders obtained by laser diffraction technique. The d_{50} and d_{90} of the cement were about 15 µm and 41 µm (respectively). As such, the size of the micro-Bi_2O_3 was within the range of the finer fractions of cement, while the Bi_2O_3 nanoparticles were substantially smaller than the cement particles.
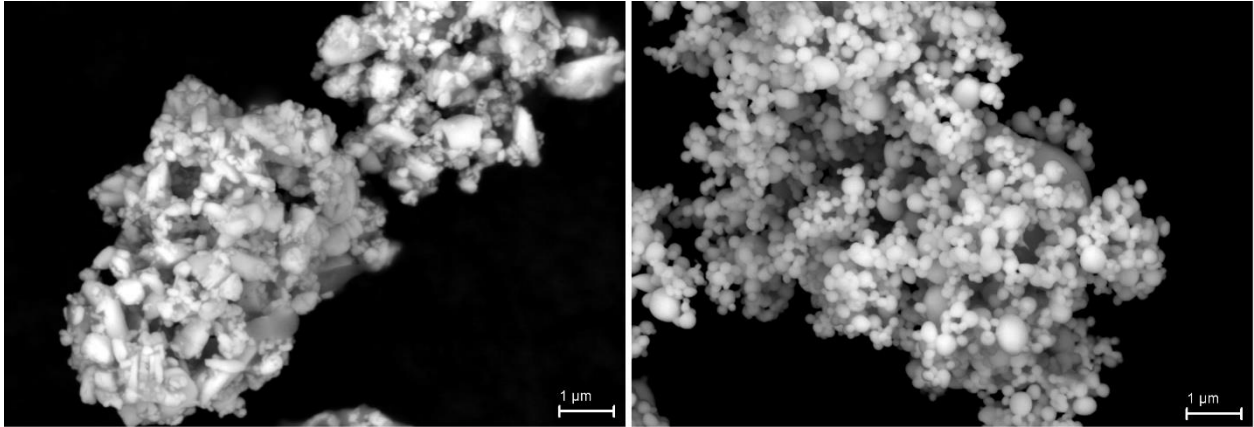
Figure 1. SEM micrographs of Bi_2O_3 microparticles (left) and Bi_2O_3 nanoparticles (right).
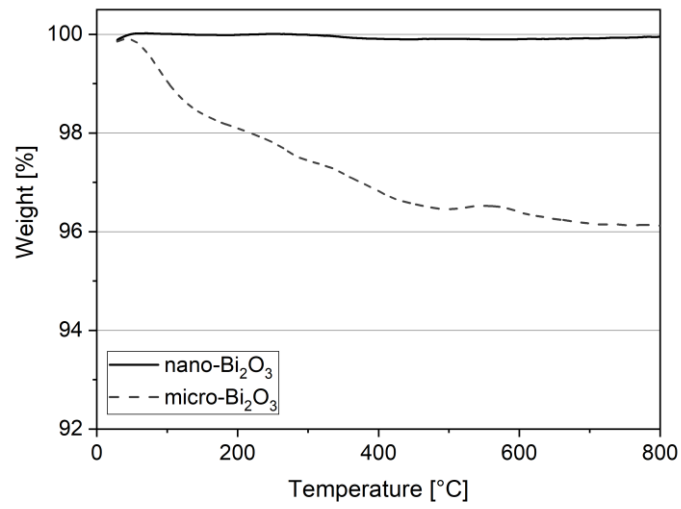

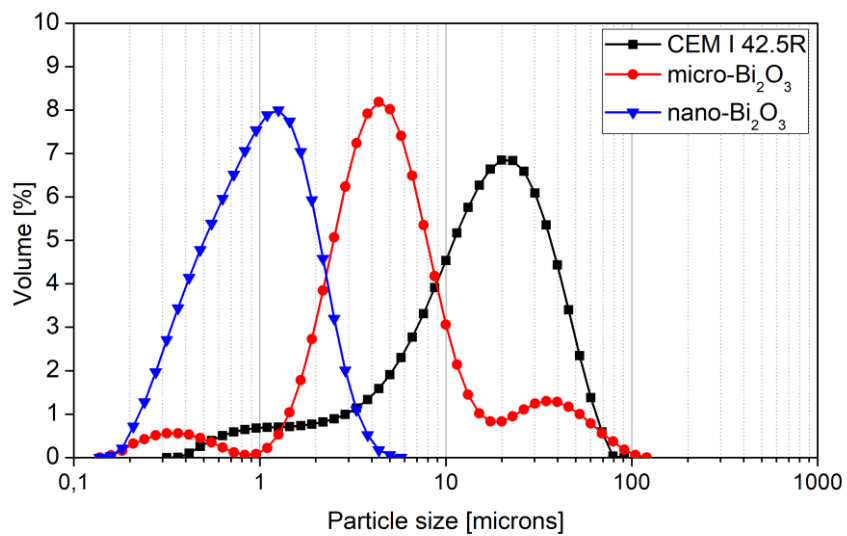Figure 2. TG curves of Bi_2O_3 micro- and nanoparticles.

Figure 3. Particle size distribution (PSD) of dry powders used for cement paste production.

2.2. Mixture compositions

Cement paste, with a water-to-binder (w/b) fixed ratio of 0.4, was produced. In total, 10 series of cement pastes, including a control (plain) paste (designated as CP), were produced. Five series of cement pastes containing 5, 10, 15, 20 and 30 wt.-% nano-Bi_2O_3 as a cement replacement, were also produced, as well as four series of cement pastes containing 5, 10, 15 and 20 wt.-% micro-Bi_2O_3 as a cement replacement. A specimen containing 30 wt.-% Bi_2O_3 microparticles was not produced, due to problems achieving the desired consistency (see section 3.2). The series of specimens containing Bi_2O_3 microparticles was designated as group BMP, while the series containing Bi_2O_3 nanoparticles was designated as BNP. The digit next to the letter designates the weight percentage of the number of particles replaced with cement. The mixture composition of the cement pastes is summarized in Table 2.

Table 2. Cement paste mix design

Paste	Cement [g]	Water [g]	Bi$_2$O$_3$ microparticles [g]	Bi$_2$O$_3$ nanoparticles [g]
CP	1000	400	0	-
BMP5	950	400	50	-
BMP10	900	400	100	-
BMP15	850	400	150	-
BMP20	800	400	200	-
BNP5	950	400	-	50
BNP10	900	400	-	100
BNP15	850	400	-	150
BNP20	800	400	-	200
BNP30	700	400	-	300

2.3. Mixing procedure and testing methods

To prepare the cement pastes, a standard mixer complying with EN 196-1 was used. For the control mix, cement and water were mixed using the following procedure: (1) slow mixing— 30 s, (2) fast mixing—1 min, (3) pause—1 min, (4) fast mixing—1 min. For other mixes, cement and Bi$_2$O$_3$ micro-/nano-particles were dry mixed for 30 seconds to ensure the homogeneous distribution of fine particles. Thereafter, the same procedure as the control mix was conducted to produce the pastes. Afterwards, the consistency of the pastes was determined with the flow table method (EN 1015-3). The spread diameter was measured twice; firstly, after removing the cone (no strokes applied) and secondly after 15 strokes of the flow table. 20×20×20 mm^3 specimens were cast for compressive strength and radiation shielding evaluations, while 40×40×40 mm^3 specimens were produced for determination of water accessible porosity. After casting, the specimens were kept in a climate chamber until the day of testing, at room temperature (20+1 °C) and at a relative humidity of 95 %. The compressive strength of the specimens was determined on 6 specimens of each series after 7 and 28 d of curing. After 28 d of curing, mercury intrusion porosimetry (MIP) tests were performed with the use of Pascal 140 and 240 series (Thermo Scientific) mercury intrusion porosimeters. The mercury density was 13.55 g/mL, the surface tension was taken as 0.48 N/m, while the selected contact angle was 140°. Before testing, small-cored specimens taken from the samples were

immersed in isopropanol and then freeze-dried, to stop hydration. Water accessible porosity was measured after 28 d of curing, merely using the water displacement method on 3 specimens from each series.

2.4. Measurement of gamma-ray and slow neutron attenuation coefficients

A "good geometry" transmission method was used for gamma-ray and slow neutron attenuation measurements. When the geometry is good, no scattered photons or neutrons reach the detector, and therefore, no correction is needed for build-up.

For the gamma-ray measurements, a scintillation spectroscopy detection system, consisting of a 2″ x 2″ NaI (TI) inorganic crystal with a 12.5 % resolution at 662 keV coupled with a multi-channel analyzer (MCA), was used to measure and record the gamma-ray spectrum. The samples were placed on specimen holder at a distance of 10 cm from source, while the source was kept at 19 cm from the detector. Point radioactive sources ^{133}Ba, ^{60}Co, ^{137}Cs, and ^{232}Th with activities of 10 mCi were used for irradiation and for energy and efficiency calibration. A lead collimator with a diameter of 3-mm was employed in order to achieve narrow-beam geometry. Finally, Genie 2000 Spectroscopy Software was used for detector calibration, data acquisition, determination of region of interest and analysis of gamma–ray spectrum. Figure 4 shows the schematic diagram of the experimental setup for the gamma-ray attenuation measurements.
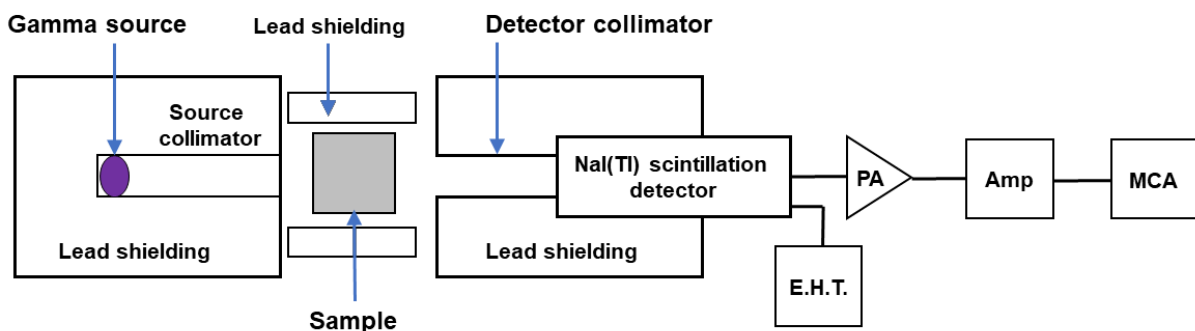

Figure 4. Gamma-ray attenuation measurement experimental setup.

The attenuation coefficients for the paste samples were obtained for gamma energy lines 80, 238.63, 662, 911, 1173.23 and 1332.49 keV, emitted from the standard radioactive sources

[131]Ba, ^{137}Cs and [60]Co. These standard sources were also used for energy and efficiency calibration of the detection system.

To deduce the values of the linear attenuation coefficient, μ, the incident (I_0) and transmitted (I) intensities of photons were measured and their values used in Beer's law (Eq. 1) [48]:

$$\mu = \frac{1}{x} ln(I_0/I) \tag{1}$$

where x is the material thickness (in cm).

Since μ is dependent upon the attenuating medium density, its value depends on the matter phase (solid, liquid, or gas). Therefore, a normalization of the linear attenuation coefficient per unit density, μ/ρ, is preferred in shielding analysis (Eq. 2).

$$\mu/\rho = \frac{1}{t} ln(I_0/I) \tag{2}$$

where t is the sample mass thickness (cm^2/g).

The theoretical values of the mass attenuation coefficients of the paste samples obtained by use of the WinXCom program [49], are also given in this study for comparison.

Regarding slow neutron measurements, an [241]Am-Be point neutron source with an activity of 3.7 GBq and a neutron yield = $(1.1\text{-}1.4) \times 10^7$ n/s, as well as a BF_3 neutron detector, were used. The [241]Am-Be point neutron source was enclosed in a metal housing with a shape of hollow cylinder with inner and outer diameters of 1.1 cm and 3.9 cm, respectively. The collimated neutron beam was slowed down with a fixed-size high-density polyethylene block prior to irradiation of the paste samples. The effective thickness of perforated paraffin wax was 11.5 cm and the natural boron concentration was 30 % by weight in paraffin. The distance between the axis of the source and the center of the detector was 73 cm. The source and detector were located 168 cm above the ground in a large room to reduce the contributions of reverse scattering as much as possible. Measurement time was kept at 400 s, for all samples, which is sufficient to achieve an acceptable degree of statistical error. The reported values are the mean value of ten measurements. The schematic diagram of the experimental setup is shown in Figure 5.

Similarly, the slow neutron macroscopic cross section Σ_{Slow} is given by Eq. 3:

$$\Sigma_{Slow} = \frac{1}{x} ln(\varphi_0/\varphi) \tag{3}$$

where φ_0 and φ are the incident and transmitted fluxes of slow neutrons, respectively.
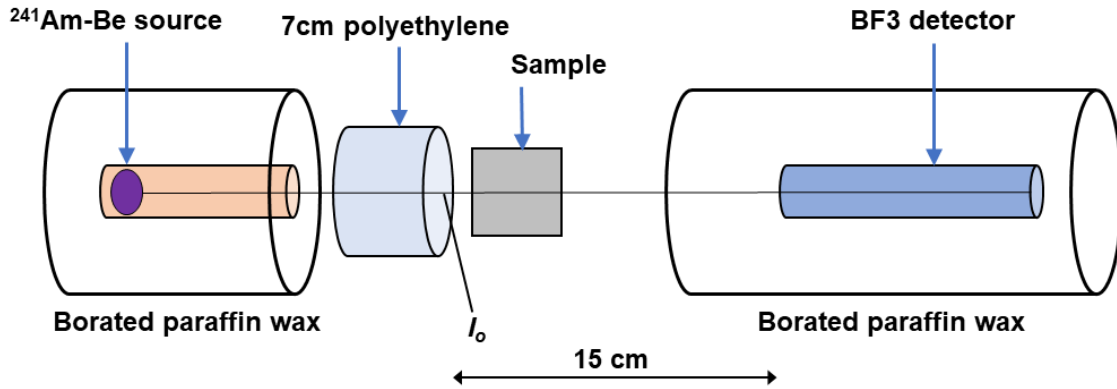

Figure 5. Schematic diagram of the experimental setup for neutron detection

Firstly, it is important to ensure that Beer's law is obeyed for the specimen thickness under consideration [50]. As such, for a given photon energy $ln(I_o/I)$ is plotted as a function of paste thickness. All plots were straight lines, indicating the validity of Beer's law. So, the μ values determined from the straight-lines fit at 80, 238.63, 662, 911, 1173.23 and 1332.49 keV. By way of example, Figure 6 illustrates the plot of $ln(I_o/I)$ against the thickness of BNP15, at 911 keV. The validly of Beer's law was also tested for a slow neutron, by plotting $ln(\varphi_0/\varphi)$ as a function of paste thickness. Similarly, all plots were straight lines, hence Σ_{Slow} for each paste is the gradient of its line. By way of example, the case of the BMP15 specimen is presented in Figure 6 (right).
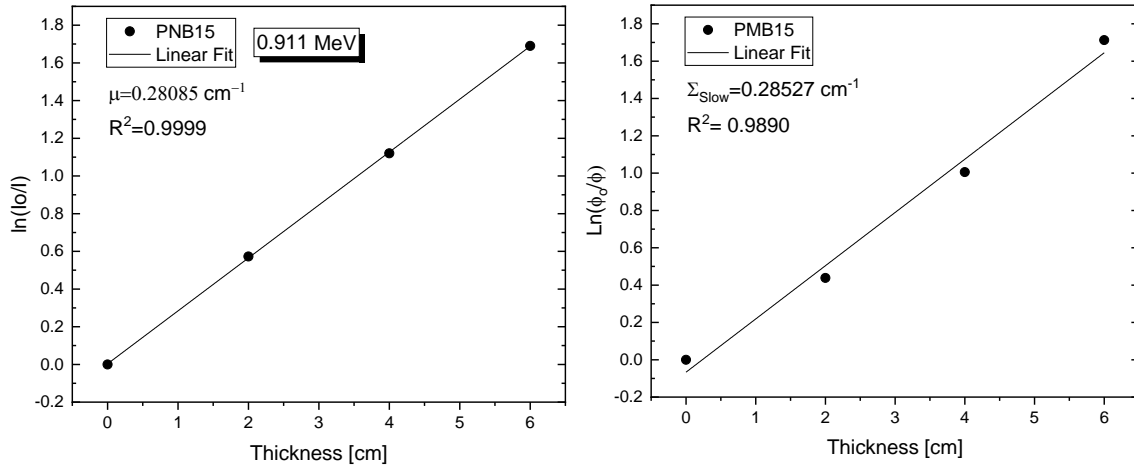
Figure 6. Variation of $ln(I_o/I)$ versus thickness for BNP15 paste sample, irradiated with 0.911 MeV gamma-ray beam (left). Variation of ln (ϕ_0/ϕ) versus thickness for BMP15 paste sample, irradiated with slow neutron beam (right).

Each experiment was repeated three times, with the average value reported. The maximum errors in μ, Σ_{Slow} and the half-value layer (HVL) were estimated using the following propagation of error formulas (Eq. 4, Eq. 5) [51]:

$$\Delta(\mu) = \frac{1}{x}\sqrt{\left(\frac{\Delta I_o}{I_o}\right)^2 + \left(\frac{\Delta I}{I}\right)^2 + \left(\frac{\Delta x}{x}\right)^2 \left(ln\left(\frac{I_o}{I}\right)\right)^2} \tag{4}$$

$$\Delta(\Sigma) = \frac{1}{x}\sqrt{\left(\frac{\Delta \varphi_o}{\varphi_o}\right)^2 + \left(\frac{\Delta \varphi}{\varphi}\right)^2 + \left(\frac{\Delta x}{x}\right)^2 \left(ln\left(\frac{\varphi_o}{\varphi}\right)\right)^2} \tag{5}$$

Since $HVL = ln\,2/\mu$ then (Eq. 6):

$$\Delta(HVL) = HVL\sqrt{\left(\frac{\Delta\Sigma}{\Sigma}\right)^2 (ln2)^2} \quad \text{or} \quad \Delta(HVL) = HVL\sqrt{\left(\frac{\Delta\mu}{\mu}\right)^2 (ln2)^2} \tag{6}$$

The estimated errors for all the radiation measurements were less than 5 %.

In this work, the authors followed the same procedure for measuring and calculating μ_m, HVL, Z_{eff}, Σ_{Slow} and Σ_R shielding parameters, as used in earlier studies [15,52].

3. Results and discussion
3.1. Consistency

The results of the consistency tests of the cement pastes are presented in Figure 7. An increment in micro-Bi_2O_3 content resulted in a dramatic decrement in their consistency, especially when the dosage was higher than 10 wt.-%. Even after 15 strokes, BMP15 and BMP20 did not reach the consistency of the reference paste (CP), in which no strokes were applied. The production of specimen BMP30 was difficult due to mixing problems i.e. the mixture was very stiff with a consistency of almost zero, making it impossible to pour the paste into molds. As a result, to avoid the addition of plasticizers which can affect composites' radiation properties, specimen BMP30 was omitted. In contrast, the addition of nano-Bi_2O_3 powder resulted in a negligible effect on the consistency of the cement pastes; indeed, a slight increment in consistency was found in pastes BNP20 and BNP30. Despite the slight increment, no bleeding was reported in any of the nano-Bi_2O_3 incorporated specimens. As can be seen in Figure 3, the size of the Bi_2O_3 microparticles was similar to that of the cement particles. Mixtures with higher dosages of micro-Bi_2O_3 had narrow particle size distributions, which resulted in low packing of particles with similar sizes. In other words, there was a high volume of pores between particles that required more water to fill the pores. Consequently, consistency was dramatically reduced as a result of an increase in the replacement level. In contrast, the addition of nano-Bi_2O_3 did not have a negative effect on the consistency. As can be seen in Figure 3, the size of nano-Bi_2O_3 was very small compared to the cement particles. The particle size of the mixture widened with the addition of the Bi_2O_3 nanoparticles, resulting in significantly improved packing density. As can be seen in Figure 7, as a result, the volume of voids between particles was minimized, and excess water was available in the pore solution to improve consistency.
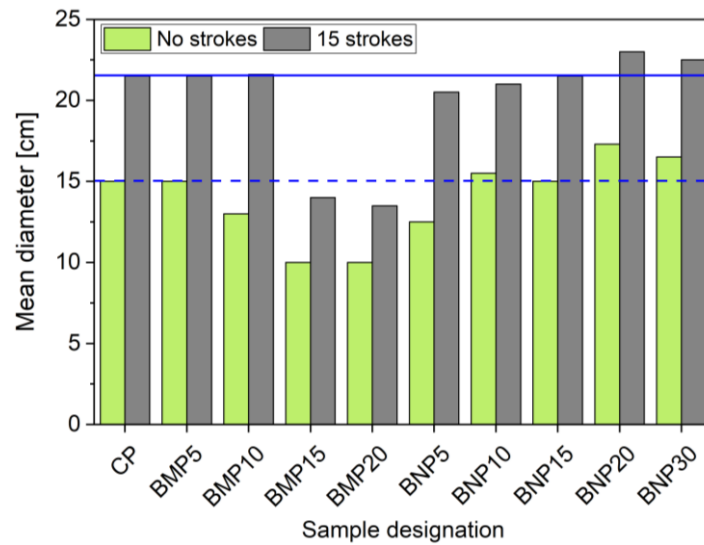
Figure 7. Consistency of cement pastes determined with the flow table method.

3.2. Compressive strength

The compressive strength of specimens after 7 and 28 d of curing is presented in Figure 8. Significant differences between the performance of the specimens containing nano and micro-powders can be distinguished. Incorporation of micro-Bi_2O_3 resulted in a gradual decrement in compressive strength after 7 and 28 d of curing, as the dosage of powder was increased. In contrast, the incorporation of a low dosage of nano-Bi_2O_3 (specimen BNP5) maintained the compressive strength of the cement paste. This effect can be attributed to the significantly smaller particle size of nano-Bi_2O_3, compared to that of cement, which results in filling of the cement matrix (the so-called nano-filling effect) [53]. This is a common phenomenon which occurs when a low dosage of nanoparticles is incorporated in cementitious composites. However, although an increment in the nano-Bi_2O_3 dosage resulted in a gradual strength decrement, modification of cement pastes with nano-Bi_2O_3 resulted in pastes having higher compressive strengths compared to pastes containing micro-Bi_2O_3. Thus, after 28 d of curing, specimen BNP30 exhibited comparable strength to that of specimen BMP20.
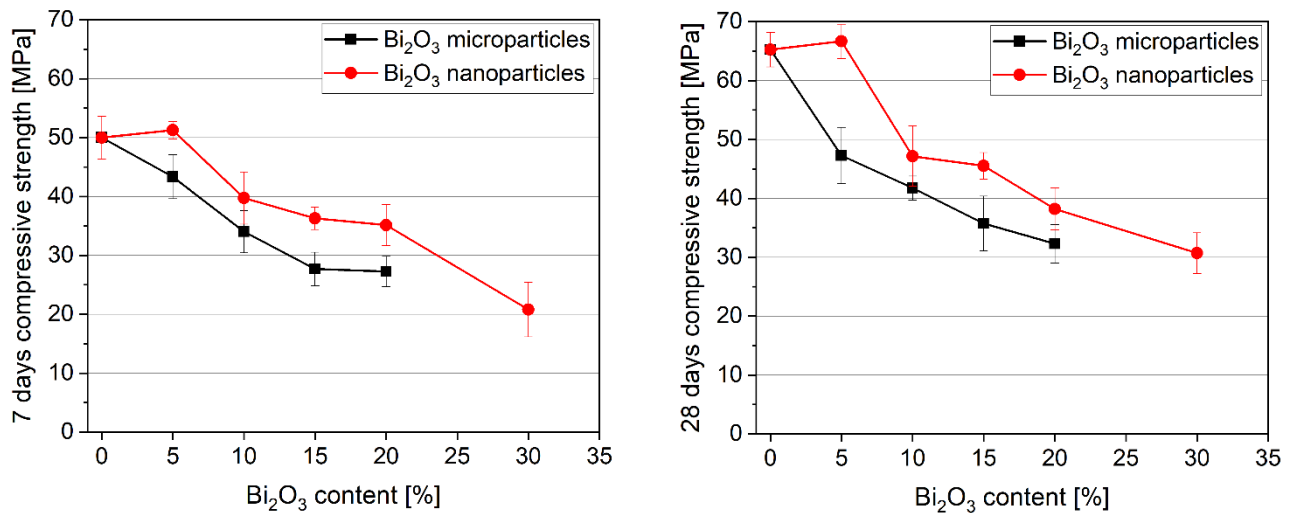
Figure 8. Compressive strength of cement pastes at 7 d (left) and 28 d (right)

However, it should be noted that in general, the incorporation of both nano-Bi_2O_3 and micro-Bi_2O_3 powders (especially in amounts > 5 wt.-%) resulted in noticeable strength reductions. Therefore, after 28 d of curing, specimens BMP10 and BNP10 exhibited compressive strengths only slightly 70% over those of the control specimens. What is more, specimens with the highest Bi_2O_3 powder contents – BMP20 and BNP30 – exhibited only about half of the compressive strength of the control specimen.

The strength loss associated with an increment in Bi_2O_3 powder dosage is in good agreement with the results from Coomaraswamy et al. [27], where Portland cement-based pastes were modified with microsized Bi_2O_3 powder. In general, it has been reported that Bi_2O_3 powder is an inert filler and is not chemically incorporated in hydration products [54,55]. Due to weak bonding between Bi_2O_3 and cement particles, an increment in the Bi_2O_3 dosage results in strength retrogression [30]. However, due to the finer particle size of nano-Bi_2O_3, compared to micro-Bi_2O_3, the nanosized particles partially filled the voids in the cement paste and somehow improved the particle size distribution within the matrix. As a result, the strength loss of specimens containing nano-Bi_2O_3 was lower than that of those containing coarser powder.

In contrast, studies on the effects of Bi_2O_3 powders on the performance of concretes [31,32] have shown that, up to a certain amount of Bi_2O_3 addition, compressive strength can be

improved. Because of the coarse aggregates, the shear during mixing is much higher and this could desagglomerate the agglomerates in the powder. Bi_2O_3 powder can thus act more effectively as a filler. In order to understand the mechanism underlying this phenomenon, mercury intrusion porosimetry tests were performed, as discussed below.

3.3. Microstructural characteristics

The results of the MIP measurements are summarized in Table 3 and depicted in Figure 9. The incorporation of micro-Bi_2O_3 powder resulted in a gradual increment in the total porosity of specimens, as well as in an increment in the average and median pore of the specimens. It is known that porosity is one of the critical parameters directly affecting the strength and durability of cement-based materials [56,57]. Accordingly, it can be seen that in the case of BMP15 and BMP20, porosities were over 50 % higher as compared with the CP specimens, with the observed results being in good correlation with compressive strength values after 28 d of curing. In addition, the porosity curve (Figure 10) is shifted to the region of larger pores (BMP15 and BMP20). A similar phenomenon was found in the case of nano-Bi_2O_3, but its deterioration rate was lower when compared to micro-Bi_2O_3. In general, up to 20 wt.-% of relative low increment of total porosity was observed. In the case of specimen BNP5, where compressive strength remained comparable to that of the CP specimen, the total porosity of the cement paste increased slightly, although the median pore diameter decreased somewhat. Therefore, it seems that despite a slight increment in porosity, nanosized particles filled the voids in the cement paste and refined its microstructure. In other words, the incorporation of nano-Bi_2O_3 increases the number of small pores and reduces the number of coarse pores. In addition, the replacement of cement with a high dosage of inert Bi_2O_3 powders results in an increment in the free water content in cement paste, since less cement is available to react with the water; as a result, the porosity of a specimen increases [27,29]. This, in turn, explains the

significant reduction in the compressive strength of cement pastes when Bi_2O_3 powders are added.

Table 3. Basic parameters of pore structure measured by MIP and water accessible porosity

| Sample designation	CP	BM5	BMP10	BMP15	BMP20	BNP5	BNP10	BNP15	BNP20	BNP30
Porosity by Hg intrusion [%]	21.09	24.85	28.08	30.72	32.82	23.27	24.34	25.15	25.56	30.99
Total pore volume [mm³/g]	121.00	147.69	169.22	178.06	203.16	131.15	133.50	135.77	141.61	162.84
Average pore diameter [nm]	40.12	42.68	45.34	50.92	50.36	41.13	51.68	40.66	40.16	42.46
Median pore diameter [nm]	85.65	85.78	93.89	113.47	99.65	84.04	103.60	80.56	77.75	81.89
Water accessible porosity [%]	26.1	28.7	30.3	30.8	32.0	25.8	28.5	29.6	31.2	34.7
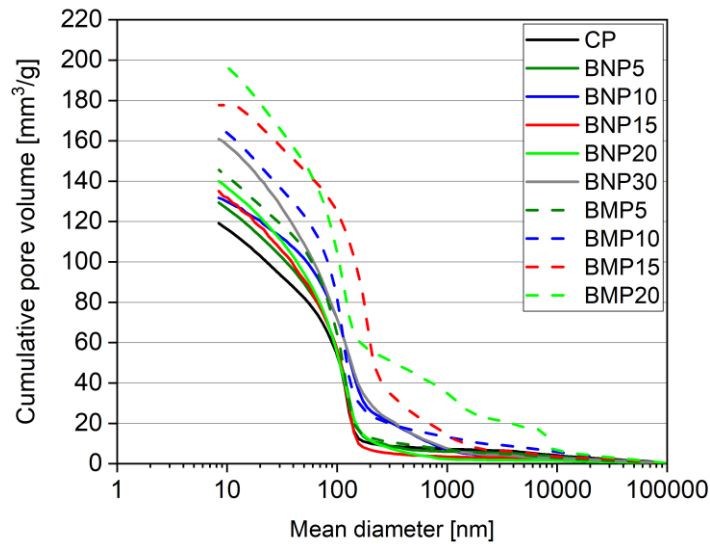
Figure 9. Cumulative pore volume of cement pastes

3.4. Water accessible porosity

The results of the water accessible porosity tests, obtained by the water displacement method, are presented in Table 3. As expected, the MIP results show that the incorporation of both types of Bi_2O_3 powders increased water accessible porosity, as a result of increased porosity of the cementitious skeleton. A similar result can be observed in the case of the water accessible porosity results. In all cases, an increased porosity was reported with an increase in the Bi_2O_3 powder dosage, though slightly higher porosity values were observed for specimens containing micro-Bi_2O_3. The highest water accessible porosity was reported for the BNP30 specimen, due to the highest proportion of cement replacing Bi_2O_3 powder. A small decrement in water

accessible porosity was found only in specimen BNP5, which confirms the idea that low nanoparticle dosages can contribute to a certain improvement in cement matrix microstructure.

3.5. Gamma-ray attenuation properties

The elemental concentrations and their densities as they occurred in the paste samples have been calculated and listed in Table S1 (Supplementary materials). The concentration values were used as input data for the WinXCom program to calculate the mass attenuation coefficients of the samples. In addition, the mean atomic number <Z>, mean atomic mass <A>, single-valued effective atomic number and its variant based on the use of different fractions, such as atomic percentage of each element (α_i^{at}), fractional electronic content (a_i^e) and the elemental weight fraction (w_i) were estimated as shown in below.

Based on the atomic percentage of each element, α_i^{at}, Manninen and Koikkalainen [58], calculate the effective atomic number as (Eq. 7):

$$Z_{\text{eff}} = \sum_i \alpha_i^{at} Z_i .$$

(7)

Where $\alpha_i^{at} = \frac{(w_i/A_i)}{\sum_i (w_i/A_i)}$.

Mayneord [59] evaluated Z_{eff} by another power law, which involves the use of the fractional electronic content (a_i^e) in the following form (Eq. 8):

$$Z_{\text{eff}} = \left(\sum_i a_i^e Z_i^{2.94}\right)^{1/2.94}$$

(8)

Finally, Murty [60] considered a simple empirical expression based on the elemental weight fraction (Eq. 9):

$$Z_{\text{eff}} = \left(\sum_i w_i Z_i^{3.1}\right)^{1/3.1}$$

(9)

Where Z and A are atomic and mass numbers, and the subscript i refers to the ith constituent element.

In fact, the availability of such the single-valued of Z_{eff} is comparatively limited for low energies and is overly simplistic for many applications. Energy-dependent effective atomic numbers, on

the other hand, provide reliable values. The energy dependence of Z_{eff} for photon interaction ($Z_{PI, eff}$) and photon energy absorption ($Z_{EA, eff}$) are given by Zayed et al. [61] (Eq. 10):

$$Z_{PI,\ eff} = \frac{\sum_i f_i A_i (\mu_m)_i}{\sum_i f_i \frac{A_i}{Z_i}(\mu_m)_i} \qquad (10)$$

Where, f_i is the fractional abundance of ith element with respect to the number of atoms ($f_i = n_i / \sum_i n_i$). To calculate $Z_{EA,\ eff}$, Eq. (10) can be used by replacing μ_m by the mass-energy absorption coefficient, ($\mu_{en,\ m}$). Table 4 lists all calculated effective atomic numbers.

Table 4. Mean atomic number, mean atomic mass, single-value of Z_{eff} calculated with different empirical expressions, maximum and minimum values of $Z_{PI,eff}$ and $Z_{PE,eff}$ are given for different Bi_2O_3 nanoparticles pastes; similar values were obtained for the microparticle cement samples.

Sample name	$<Z>$	$<A>$	Z_{eff}[a]			$Z_{PI,eff}$ (1 keV-100 GeV)		$Z_{PE,eff}$ (1 keV-20 GeV)	
			Eq. (7)	Eq. (8)	Eq. (9)	Min.	Max.	Min	Max.
CP	6.75	13.12	13.74	14.84	15.17	6.76	17.4	6.73	17.9
BNP5	6.91	13.54	18.91	25.59	28.77	6.97	23.4	6.95	25.7
BNP10	7.09	14.00	23.12	31.45	35.32	7.2	29.3	7.18	32.6
BNP15	7.29	14.51	26.82	35.91	40.12	7.46	34.6	4.75	38.8
BNP20	7.51	15.08	30.21	39.64	44.05	7.73	39.4	7.73	44.1
BNP30	8.04	16.42	36.45	45.94	50.49	8.4	47.9	8.39	52.8

Note: [a] Calculated as described by the indicated Equation.

From Table 4, all calculated parameters showed systematic increases with increasing Bi_2O_3 content. Accordingly, these preliminary calculations indicate that Bi_2O_3 addition has a significant effect on the γ-ray shielding performance of cement-Bi_2O_3 composites.

The linear attenuation coefficient of the cement paste, modified with the bismuth oxide nano and microparticles additions, were measured at 0.08, 0.238, 0.662, 0.911, 1.173, 1.333 and 2.614 MeV photon energies experimentally and theoretically calculated with WinXCom. The μ decreased with increasing photon energy for all the samples examined, but it exhibited a

significant increase with increasing Bi_2O_3 concentration (Table 5). Specimen BMP30 exhibited the highest μ values, while the lowest values were determined in the reference paste sample (CP).

Table 5 reveals that composites loaded with 30 wt.-% nano-Bi_2O_3 has increments of 363.3 % and 145.4 %, for γ -ray linear attenuation coefficients at 0.08 and 2.614 MeV, respectively.

The correlation of μ with the type of inclusion particles indicates that there was a slight increase in the linear attenuation coefficient when using microparticles, which agrees with the literature [41]. However, this shift in values can be considered negligible and within the experimental error margin, as shown in Table 5. This result, which is discussed in section 3.5.1 below, is in agreement with earlier findings in the literature [39].

Table 5. Experimental linear attenuation coefficients μ (cm^{-1}) of γ-rays of cement pastes having Bi$_2$O$_3$ micro- and nanoparticles; experimental error $\leq$ 5%.

Paste	Energy (MeV)						
	0.08	0.238	0.662	0.911	1.173	1.333	2.614
CP	0.865	0.382	0.245	0.211	0.186	0.174	0.125
BMP5	1.420	0.545	0.292	0.249	0.219	0.204	0.147
BNP5	1.350	0.550	0.280	0.237	0.211	0.192	0.146
Diff.%	-4.9	0.9	-4.2	-4.6	-3.7	-5.5	-0.7
Δ%	56.2	44.1	14.1	12.6	13.2	10.3	16.7
BMP10	1.950	0.680	0.318	0.269	0.233	0.218	0.158
BNP10	1.910	0.665	0.309	0.262	0.232	0.215	0.157
Diff.%[a]	-2.1	-2.2	-2.9	-2.4	-0.4	-1.6	-0.6
Δ%[b]	120.9	74.2	26.1	24.3	24.6	23.2	25.9
BMP15	1.975	0.835	0.349	0.290	0.252	0.235	0.170
BNP15	2.000	0.840	0.335	0.279	0.246	0.227	0.169
Diff.%	1.3	0.6	-3.9	-3.8	-2.4	-3.6	-0.9
Δ%	131.3	120.0	36.7	32.5	31.9	30.1	35.3
BMP20	3.145	1.010	0.377	0.310	0.268	0.250	0.182
BNP20	3.105	0.960	0.360	0.298	0.255	0.242	0.166
Diff.%	-1.3	-5.0	-4.6	-3.9	-5.0	-3.1	-8.8
Δ%	259.2	151.5	46.7	41.3	36.6	38.9	33.1
BNP30	4.005	1.060	0.591	0.370	0.317	0.347	0.306
Δ%	363.3	177.7	141.2	75.7	70.3	99.1	145.4

[a]Diff. [%] $= 100 \times (\mu_{\text{BNP 20}} - \mu_{\text{BMP}})/\mu_{\text{BMP}}$

[b][%] $= shielding\ improvement\ [\%] = 100 \times (\mu_{\text{BNP 20}} - \mu_{\text{CP}})/\mu_{\text{CP}}$

For validation of our results, the experimental $(\mu/\rho)_{\text{exp.}}$ and theoretical $(\mu/\rho)_{\text{theo.}}$ mass attenuation coefficients for different pastes, modified with Bi$_2$O$_3$ nano and microparticles, are depicted simultaneously in Figures 10 and 11, respectively. Given that the determination of μ/ρ dependence on photon energy is based on the corresponding dependence of partial photon interactions, the energy behavior of the mass attenuation coefficient should be discussed in terms of the relative importance of these partial photon processes. For an energy range from 80 keV to 238 keV high contributions of photoelectric absorption causes a sharp decrease in mass attenuation coefficient, as the γ-ray energy increases. At the same time, Compton scattering dominates over the other energy region (0.662-2.614 MeV), which produces a considerable or slight decrease in μ/ρ values with increasing photon energy.
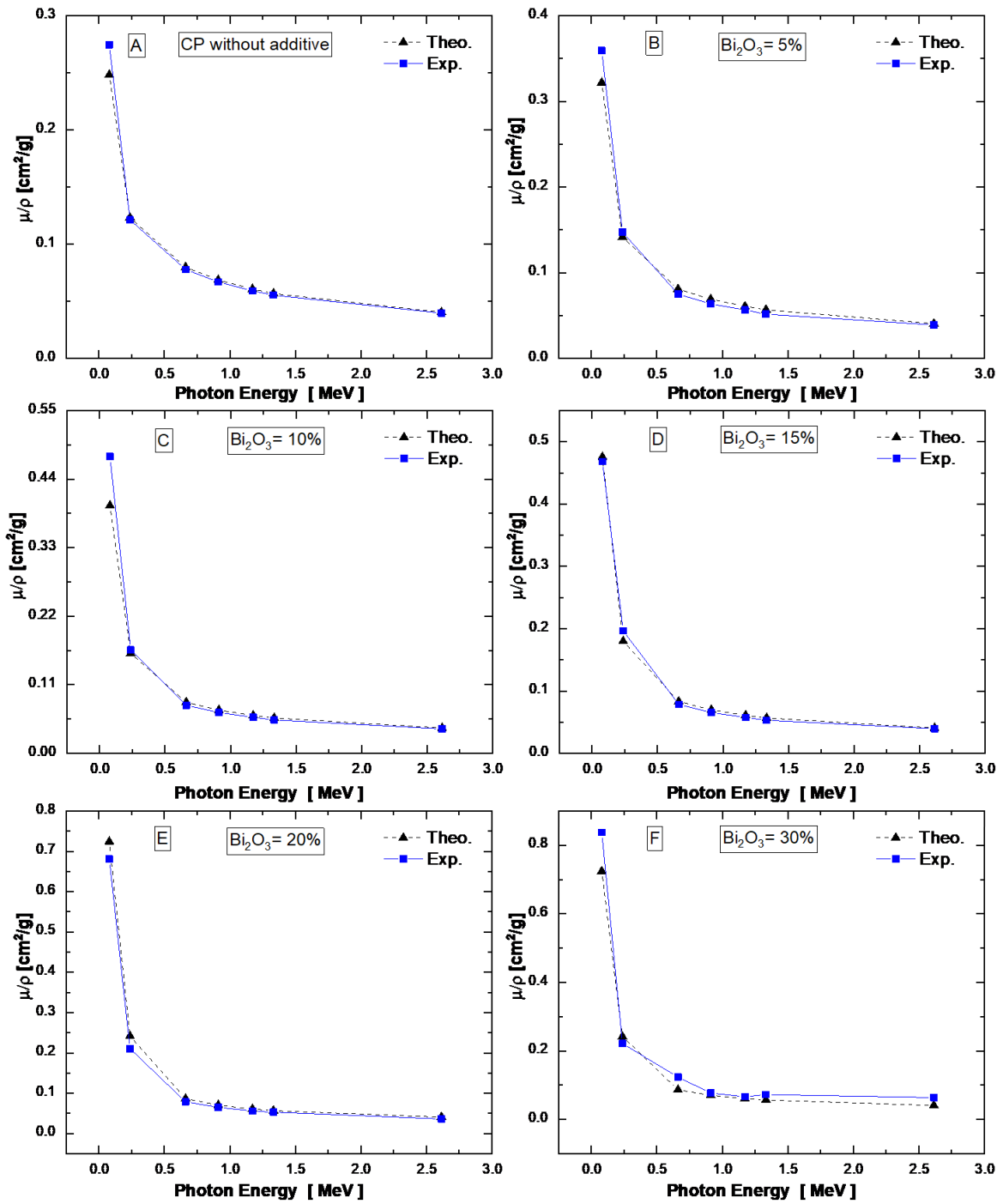
Figure 10. Experimental and theoretical mass attenuation coefficients of cement pastes: (A) CP, (B) BNP5, (C) BNP10, (D) BNP15, (E) BNP20, and (F) BNP30 as a function of photon energy.
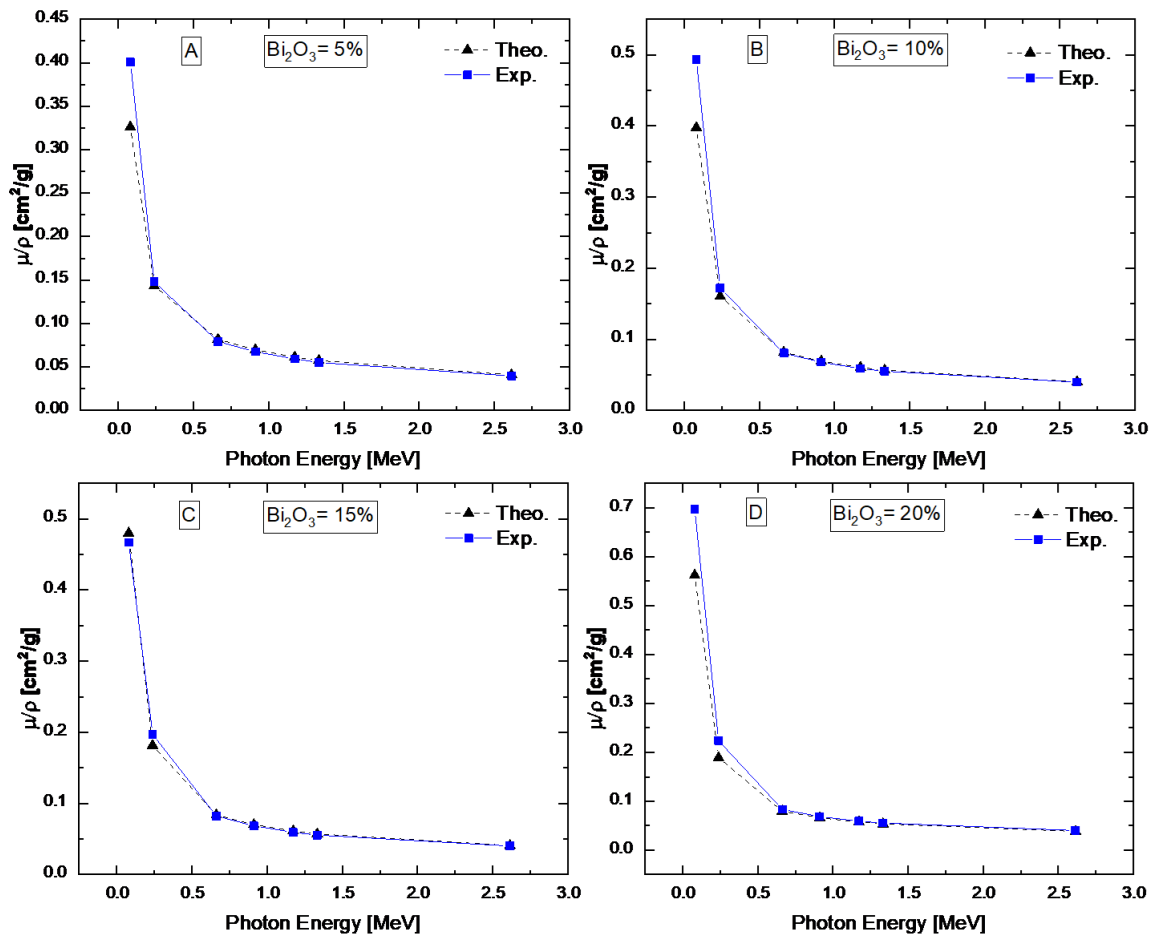
Figure 11. Experimental and theoretical mass attenuation coefficients of BMPs: (A) BMP5, (B) BMP10, (C) BMP15 and (D) BMP20 as a function of photon energy.

The experiment results for all samples agree well with the theoretical data (Figs. 10 and 11). However, (μ/ρ) measured at 0.08 MeV showed a clear deviation from the theoretical model, due to the dominance of the photoelectric process, which is highly dependent on the atomic number. As a result, measurement is sensitive to sample homogeneity, while the calculation is overly sensitive to errors in the elemental analysis. In addition, the experimental and theoretical results of samples BNP15 and BMP15, shown in Figures 10(D) and 11(C), respectively, are in very close agreement, which can be attributed to the high level of homogeneity at this bismuth concentration.

The normal way to discuss the impact of a certain additive on radiation shielding properties is through a comparison of mass attenuation coefficients of a particular material, with and without

additives. Variation in mass attenuation coefficients between the BNP20, BMP20 and CP samples, as a function of photon energy, are given in Figure 12. All three samples had μ/ρ values which were systematically higher than those of CP, especially in the low energy range. Nevertheless, no significant differences were seen in the gamma-ray attenuation performance between the nanoparticle paste series and microparticle paste series, at the same addition rate, as shown in Figure 12 (A and B).
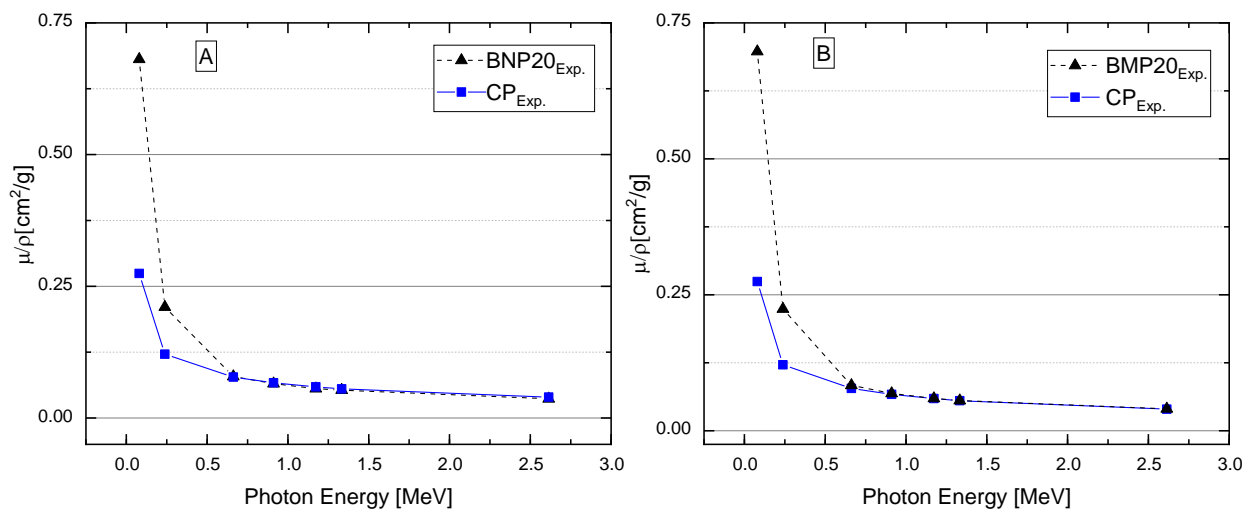

Figure 12. Experimental mass attenuation coefficients for (A) CP and BNP20 and (B) CP and BMP20, as a function of photon energy.

Another interesting observation, visible in the 80 to 238 keV energy range in Fig. 12, is that the μ/ρ of paste with additive declined faster than the control paste sample. This difference is a direct result of the fact that heavy addition extended the dominant region of the photoelectric effect in the modified paste, to higher photon energies, compared with the reference paste. For instance, the percentage probabilities of the photoelectric process in the energy interval 80 - 238 keV, ranged from 30 % to 2 % and from 69 % to 49 % for CP and BNP30, respectively. This means that whilst at 238 keV the photoelectric interaction in the CP sample was a negligible process, its effect was still significant in the BNP30 sample. Therefore, the contribution of the photoelectric process may show up as an increase in the decline rate of μ/ρ in the cement paste modified with bismuth oxide.

The half-value layer thickness (HVL) is a parameter associated with the attenuation coefficient. It stands for the material thickness that reduces the intensity of radiation by one half. Table 6, which lists the measured HVL values, indicates that pastes with higher Bi_2O_3 content had lower HVL, and therefore, those smaller thicknesses were needed. Again, as shown in Table 6, no significant difference between nano-and micronized Bi_2O_3 was observed. Even though there was a slight decrement in HVL when microparticles were used, the decrement was often insignificant or within experimental error.

Table 6. Experimental HVL (in cm) of γ-rays for Bi_2O_3 micro and nanoparticles cement pastes; with experimental errors ≤ 4%.

Sample name	HVL (cm)						
	0.08 MeV	0.238 MeV	0.662 MeV	0.911 MeV	1.173 MeV	1.333 MeV	2.614 MeV
CP	0.80	1.82	2.83	3.29	3.72	3.98	5.56
BMP5	0.49	1.27	2.38	2.79	3.17	3.41	4.73
BNP5	0.51	1.26	2.48	2.92	3.29	3.61	4.76
BMP 10	0.36	1.02	2.18	2.58	2.97	3.18	4.39
BNP 10	0.36	1.04	2.24	2.65	2.99	3.23	4.41
BMP 15	0.35	0.83	1.99	2.39	2.75	2.95	4.07
BNP 15	0.35	0.83	2.07	2.48	2.82	3.06	4.11
BMP 20	0.22	0.69	1.84	2.24	2.59	2.78	3.81
BNP 20	0.22	0.72	1.93	2.33	2.72	2.86	4.18
BNP 30	0.17	0.65	1.17	1.87	2.18	2.00	2.27

Part of the experiment was aimed at determining the relationship between the attenuation coefficient and the weight fraction of the Bi_2O_3 addition. The results for the nano- and micro-Bi_2O_3 were similar. Because a simple relationship between the attenuation coefficient and the Bi_2O_3 loading, over the full energy range considered (i.e., $0.8 \leq E \leq 2.614$ MeV), does not exist, the results have been presented for two separate energy regions: (A) over the energy range 0.08-0.238 MeV, where photon interactions were sheared between photoelectric and Compton scattering and (B) over the energy range (0.911-2.614 MeV), in which Compton scattering was dominant. For our samples, the relationships over the two energy regions were markedly linear,

for both nano- and microparticles additions. Only the results for the nano-Bi_2O_3 cement paste series have been presented here (Fig. 13).
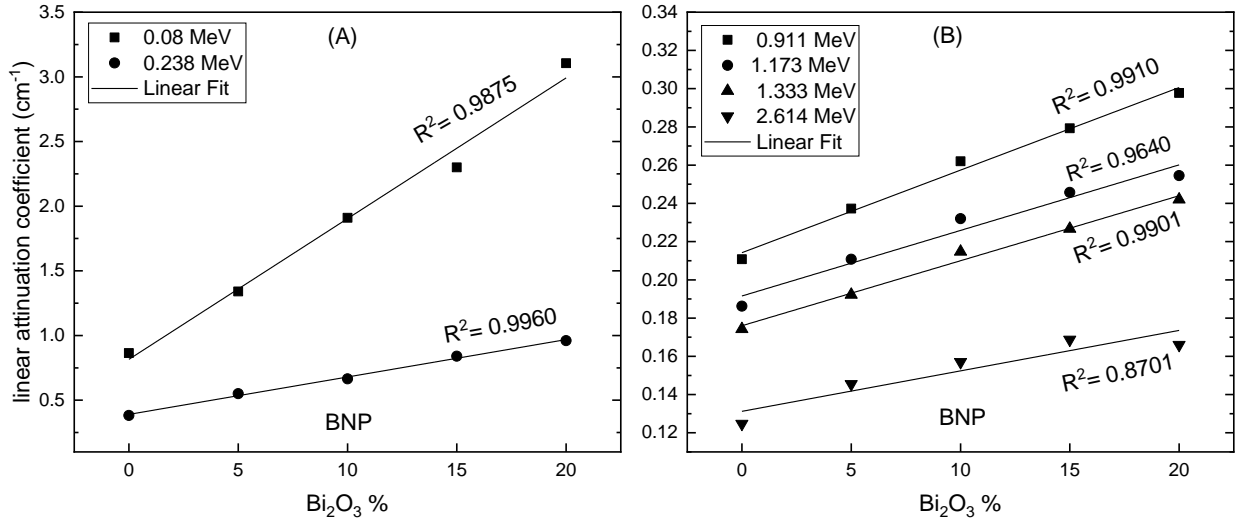

Figure 13. The linear attenuation coefficient of Bi_2O_3 nanoparticle cement paste as a function of weight percentage of Bi_2O_3, over two energy regions: (A) (0.08-0.238 MeV) and (B) (0.911-2.614 MeV).

3.5.1. Comparison with published studies

The results presented above concern the size and loading effects of Bi_2O_3 particles on γ-ray absorption, in nano-sized and micro-sized Bi_2O_3-cement paste composites. The results demonstrate that the size effect on γ-ray attenuation was insignificant at various photon energies (i.e., 0.08 –2.614 MeV). Our results are in line with many earlier experimental studies, which underline that γ-ray transmissions in both nano-sized and micro-sized particles are remarkably similar at photon energies > 30 keV. For instance, in works [36,39] the authors reported that for WO_3-epoxy composites, the size effect (nano or micro) becomes insignificant at photon energies between 30 to 40 keV. Aghaz et al. [40] have also shown that diagnostic X-rays, measured at 80 and 100 kVp tube voltages, lead to an almost unchanged dose after passing through both nano- and micro-structured WO_3/PVC samples. Künzel and Okuno [37] have published comparable results about the effects of the particle sizes of CuO compounds on X-

ray absorption. These studies support only the superiority of X-ray absorption by nanostructured materials, as compared to microstructured ones, at low energy X-ray beams. Such results confirm that the superiority of nano-sized materials, over their micro-sized counterparts, is highly dependent on photon energy and is only seen at lower energies (i.e.,< 30 keV). Beyond 60 keV, however, the size effect becomes negligible [62] and as a result, an almost γ-ray like shielding capability, for both nano and micro-structured samples, can be expected. Moreover, in a study by Shik and Gholamzadeh [41] it was found that a decrease in HVL, with energy for the PbO/EPVC microparticle composites, is not as steep as for their nano-sized counterparts. As such, they conclude that shields fabricated with microparticles can better attenuate photons with higher energies.

In contrast to experimental results, there have been some theoretical studies based on the Monte Carlo (MC) simulation, in which researchers such as Tekin et al. [34] and Verdipoor et al. [35] have argued for the superiority of nanostructured materials at higher photon energies. Such unexpected simulation results, which contradict experimental data, can be explained by two main factors. Firstly, there is the issue of the validity of using the simple mixture rule to predict the physical properties of complex, real samples. In other words, the MC or WinXCom program does not consider, for example, microstructural defects due to voids or agglomerates. Secondly, the cross-sectional library is limited to elements, instead of compound cross-sections. This approach treats the specimen as a group of isolated elements, without considering molecular or solid-state effects which modify cross-section values in real materials. The results of this research thus suggest that careful interpretation must be undertaken for attenuation properties obtained theoretically, because theoretical models oversimplify the radiation attenuation problem, by neglecting the influence of microstructural effects that occur in real materials [63].

3.6. Neutron attenuation properties

The macroscopic cross-section of slow neutrons (with energies higer than 0.5 eV), Σ_{Slow}, was measured for all paste samples, with the effective removal cross-sections of fast neutrons, Σ_R, calculated with the NXCom program [64]. Moreover, the associated HVL values were also determined, with all the results of neutron shielding property tests presented in Table 7.

As can be seen in Table 7, no simple relationship exists between slow neutron attenuation and Bi_2O_3 loading, but there were improved values for Σ_{Slow} at specific loading rates (5 % and 10 %). The composite loaded with 30 wt.-% nano-Bi_2O_3 shows a distinct increment of 33 % for the Σ_{Slow} over the reference paste. Irregularities in the variations of Σ_{Slow} with increases in Bi_2O_3 content can be attributed to microstructural effects. This is because the total neutron cross-section of the Bi-209 nucleus, at slow neutron energies (0.5-10 eV), is not high enough to produce a notable change in Σ_{Slow} (see Figure S1 – Supplementary materials).

The removal cross-section results showed a systematically increasing trend, with an increasing additive ratio. This behavior can be explained in terms of chemical composition and the total neutron cross-section of Bi-209 due to neutron capture at the resonance region (Figure S1) and scattering interactions (Figure S2 – Supplementary materials) at fast energies (10 keV-10 MeV). Both effects increase the removal cross-section as bismuth content increases.

Table 7 also shows the correlation between the inclusion particle type and the attenuation coefficients for slow and fast neutrons. It can be seen that, except for BNP30, both Σ_{Slow} and Σ increased only slightly when nanoparticles were used. The slight differences between the micro- and nanoparticle additions could have originated from structural or physical properties like density or paste porosity.

Table 7. Experimental macroscopic cross-sections of slow neutron Σ_{Slow} and the calculated removal cross-section of fast neutron Σ_R for micro-and nanoparticles cement pastes. The corresponding HVLs are listed.

Paste	Σ (cm^{-1})				HVL (cm)			
	Σ_{Slow}	[%]^a	Σ_R	[%]	Slow	[%]	Fast	[%]
CP	0.2853±0.0096		0.162		2.430±0.023		4.27	
BMP5	0.2860±0.0100	0.3	0.185	13.75	2.424±0.024	-0.3	3.76	-11.9
BNP5	0.2898±0.0104	1.6	0.187	15.29	2.392±0.025	-1.6	3.71	-13.1
BMP 10	0.2940±0.0109	3.0	0.192	18.62	2.358±0.026	-3.0	3.6	-15.7
BNP 10	0.2977±0.0113	4.3	0.195	20.41	2.328±0.026	-4.2	3.55	-16.9
BMP 15	0.2853±0.0111	0.0	0.2	23.18	2.430±0.027	0.0	3.47	-18.7
BNP 15	0.2872±0.0115	0.7	0.202	24.35	2.414±0.027	-0.7	3.44	-19.4
BMP 20	0.2850±0.0117	-0.1	0.206	27.19	2.432±0.028	0.0	3.36	-21.3
BNP 20	0.2874±0.0121	0.7	0.209	28.55	2.411±0.029	-0.8	3.32	-22.2
BNP 30	0.3795±0.0227	33.0	0.204	25.46	2.430±0.035	-24.8	3.41	-20.1

^{a}[%] = $shielding\ improvement$ [%] = $100 \times (\Sigma_{BNP} - \Sigma_{CP})/\Sigma_{CP}$

The correlation between the inclusion particle type and neutron attenuation was in contrast with the results of γ-ray attenuation; i.e., the microparticles caused a slight increase in γ-ray shielding properties, in comparison with the nanoparticles (see Table 5). This difference confirms the accuracy of our experiment because gamma and neutron shielding materials tend to have opposite requirements concerning their constituents.

Finally, the fast and slow neutron HVL results showed similar variation trends to Σ_{Slow} and Σ_R. No simple relation describes the variation of HVL (slow) with the Bi_2O_3 loading rate. However, for the fast neutron, the CP was worse by ~25 % in neutron shielding performance, expressed as HVL (fast), in relation to BNP30, as shown in Table 7.

4. Conclusions

In this study, Bi_2O_3 micro and nanoparticles were evaluated as potential Portland cement replacements for producing a lead-free shielding material. A comparative study between these pastes was carried out regarding their physical, mechanical and radiation shielding properties. The following conclusions can be drawn from the theoretical and experimental findings above:

1) The particle size distribution of Bi_2O_3 has a significant influence on water demand as well as on cement paste consistency. It affects packing density at the level of fine particles and consequently plays an important role in determining paste consistency. Incorporation of more than 10 wt.-% of micro-Bi_2O_3 to the paste resulted in a dramatic decrement in their consistency. In contrast, specimens with nano-Bi_2O_3 exhibited slight consistency decrement even when cement was replaced up to 30 wt.-% with nano-Bi_2O_3.

2) Replacement of cement with Bi_2O_3 micro- and nanoparticles results in a gradual decrement in the compressive strength of cement pastes. However, the deterioration rate varies, depending on the type of powder used, in favor of nano-Bi_2O_3. Replacement of cement with 20 wt.-% of micro-Bi_2O_3 resulted in decrement of 28 d compressive strength by half. Similar strength loss was reported when cement was replaced with 30 wt.-% of nano-Bi_2O_3. In addition, a small dosage (5 wt.-%) of nano-Bi_2O_3 prevents strength loss, due to the filling ability of nanoparticles.

3) Similarly, the incorporation of micro-Bi_2O_3 powder resulted in a gradual increment of the total porosity and water accessible porosity of cement paste. The specimens containing 15 wt.-% and 20 wt.-% of micro-Bi_2O_3 exhibited over 50 % higher total porosities than control specimen. In case of nano-Bi_2O_3, up to 20 wt.-% relatively low increment of total porosity was observed. However, specimen containing 30 wt.-% of nano-Bi_2O_3 exhibited 47 % higher total porosity than control specimen.

4) All γ-shielding parameters show systematic increases with increasing Bi_2O_3 content. However, the role of particle size in γ-ray shielding was insignificant over the energy range of interest (i.e. 0.08-2.614MeV). It seems, however, that this finding is in line with the findings of many earlier experimental studies.

5) The experimental and theoretical results of BNP15 and BMP15 sample tests were in excellent agreement.

6) Bi_2O_3 addition extended the dominant region of the photoelectric process in the modified paste to higher photon energies, compared with the reference paste.

7) No simple relationship exists between the linear attenuation coefficient and Bi_2O_3 loading, over the energy range of interest. However, variations in μ for nano and microparticles are markedly linear for two energy regions; (0.08-0.238 MeV), and (0.911-2.614 MeV).

8) Careful interpretation must be undertaken regarding radiation attenuation properties obtained theoretically. This is because theoretical models oversimplify the attenuation problem, by neglecting the influence of the molecular and microstructural effects that are found in real samples.

9) Due to the presence of microstructural effects, no simple relationship exists between slow neutron attenuation and Bi_2O_3 content. However, improved values for Σ_{Slow} were observed at specific loading rates (5 wt.-% and 10 wt.-%). Furthermore, a distinct value was found for BNP30.

10) The Σ_R results showed systematic increase with an increasing Bi_2O_3 ratio.

References

[1] Al-Buriahi MS, Sriwunkum C, Arslan H, Tonguc BT, Bourham MA. Investigation of barium borate glasses for radiation shielding applications. Appl. Phys. A 2020;126(1). https://doi.org/10.1007/s00339-019-3254-9.

[2] Hernandez-Murillo CG, Molina Contreras JR, Escalera-Velasco LA, Leon-Martínez HA de, Rodriguez-Rodriguez JA, Vega-Carrillo HR. X-ray and gamma ray shielding behavior of concrete blocks. Nuclear Engineering and Technology 2020;52(8):1792–7. https://doi.org/10.1016/j.net.2020.01.007.

[3] Escalera-Velasco LA, Molina-Contreras JR, Hernández-Murillo CG, León-Martínez HA de, Vega-Carrillo HR, Rodríguez-Rodríguez JA et al. Shielding behavior of artisanal bricks against ionizing photons. Appl Radiat Isot 2020;161:109167. https://doi.org/10.1016/j.apradiso.2020.109167.

[4] A.J. Al-Saadi, A.K. Saadon, Gamma Ray Attenuation Coefficients for Lead Oxide and Iron Oxide Reinforced In Silicate Glasses as Radiation Shielding Windows, Ibn Al-Haitham Jour. for Pure & Appl. Sci. 27 (2014).

[5] H.A. Saudi, Lead Phosphate Glass Containing Boron and Lithium Oxides as a Shielding Material for Neutron- and Gamma-Radiation, Applied Mathematics and Physics 1 (2013) 143–146. https://doi.org/10.12691/amp-1-4-7.

[6] E. Kavaz, N. Ekinci, H.O. Tekin, M.I. Sayyed, B. Aygün, U. Perişanoğlu, Estimation of gamma radiation shielding qualification of newly developed glasses by using WinX-COM and MCNPX code, Progress in Nuclear Energy 115 (2019) 12–20. https://doi.org/10.1016/j.pnucene.2019.03.029.

[7] A.B. Azeez, K.S. Mohammed, M.M.A.B. Abdullah, N.N. Zulkepli, A.V. Sandu, K. Hussin, A. Rahmat, Design of flexible green anti-radiation shielding material against gamma-ray, Materiale Plastice 51 (2014) 300–308.

[8] Marquez-Mata CA, Mata Chavez MJ, Campillo-Rivera GE, Vazquez-Bañuelos J, Garcia-Duran A, Vega-Carrillo HR. Shielding features of seven types on natural quartz. Appl Radiat Isot 2021;167:109450. https://doi.org/10.1016/j.apradiso.2020.109450.

[9] Jóźwiak-Niedźwiedzka D, Glinicki MA, Gibas K, Baran T. Alkali-Silica Reactivity of High Density Aggregates for Radiation Shielding Concrete. Materials (Basel) 2018;11(11). https://doi.org/10.3390/ma11112284.

[10] M. Techman, S. Skibicki, Use of DMDA method for production of heavyweight concrete, MATEC Web Conf. 219 (2018) 3011. https://doi.org/10.1051/matecconf/201821903011.

[11] León-Martínez HA de, Molina-Contreras JR, Escalera-Velasco LA, Hernández-Murillo CG, Vega-Carrillo HR, Rodríguez-Rodríguez JA. Shielding capabilities study of light-gray, pale-pink and orange-pink Zacatecan quarries against ionizing photons using EDXRF and XCOM code. Progress in Nuclear Energy 2020;123:103287. https://doi.org/10.1016/j.pnucene.2020.103287.

[12] J. de Brito, N. Saikia, Recycled Aggregate in Concrete, Springer London, London, 2013.

[13] A. Mesbahi, H. Ghiasi, Shielding properties of the ordinary concrete loaded with micro- and nano-particles against neutron and gamma radiations, Appl. Radiat. Isot. 136 (2018) 27–31. https://doi.org/10.1016/j.apradiso.2018.02.004.

[14] S.A.M. Issa, A.M.A. Mostafa, Effect of Bi2O3 in borate-tellurite-silicate glass system for development of gamma-rays shielding materials, Journal of Alloys and Compounds 695 (2017) 302–310. https://doi.org/10.1016/j.jallcom.2016.10.207.

[15] A.M. El-Khayatt, H.A. Saudy, Preparation and characterization of zinc, lanthanum white sand glass for use in nuclear applications, Radiation Physics and Chemistry 166 (2020) 108497. https://doi.org/10.1016/j.radphyschem.2019.108497.

[16] H.A. Saudi, Gamma Ray and Neutron Shielding Properties ofBismuth Phosphate Glass Containing Iron and Barium, SOP TRANSACTIONS ON APPLIED PHYSICS 1 (2014) 1–4.

[17] P. Sikora, M. Abd Elrahman, E. Horszczaruk, P. Brzozowski, D. Stephan, Incorporation of magnetite powder as a cement additive for improving thermal resistance and gamma-ray shielding properties of cement-based composites, Construction and Building Materials 204 (2019) 113–121. https://doi.org/10.1016/j.conbuildmat.2019.01.161.

[18] W. Gallala, Y. Hayouni, M.E. Gaied, M. Fusco, J. Alsaied, K. Bailey, M. Bourham, Mechanical and radiation shielding properties of mortars with additive fine aggregate mine waste, Annals of Nuclear Energy 101 (2017) 600–606. https://doi.org/10.1016/j.anucene.2016.11.022.

[19] B. Oto, A. Gur, Gamma-ray shielding of concretes including magnetite in different rate, International Journal of Physical Sciences 8 (2013) 310–314. https://doi.org/10.5897/IJPS2013.3854.

[20] I.M. Nikbin, R. Mohebbi, S. Dezhampanah, S. Mehdipour, R. Mohammadi, T. Nejat, Gamma ray shielding properties of heavy-weight concrete containing Nano-TiO2, Radiation Physics and Chemistry 162 (2019) 157–167. https://doi.org/10.1016/j.radphyschem.2019.05.008.

[21] S.N. Yılmaz, A. Güngör, T. Özdemir, The investigations of mechanical, thermal and rheological properties of polydimethylsiloxane/bismuth (III) oxide composite for X/Gamma ray shielding, Radiation Physics and Chemistry 170 (2020) 108649. https://doi.org/10.1016/j.radphyschem.2019.108649.

[22] V.I. Pavlenko, N.I. Cherkashina, R.N. Yastrebinsky, Synthesis and radiation shielding properties of polyimide/Bi2O3 composites, Heliyon 5 (2019) e01703. https://doi.org/10.1016/j.heliyon.2019.e01703.

[23] Al-Buriahi MS, Rashad M, Alalawi A, Sayyed MI. Effect of Bi2O3 on mechanical features and radiation shielding properties of boro-tellurite glass system. Ceramics International 2020;46(10):16452–8. https://doi.org/10.1016/j.ceramint.2020.03.208.

[24] Al-Buriahi MS, El-Agawany FI, Sriwunkum C, Akyıldırım H, Arslan H, Tonguc BT et al. Influence of Bi2O3/PbO on nuclear shielding characteristics of lead-zinc-tellurite glasses. Physica B: Condensed Matter 2020;581:411946. https://doi.org/10.1016/j.physb.2019.411946.

[25] Boukhris I, Kebaili I, Al-Buriahi MS, Tonguc B, AlShammari MM, Sayyed MI. Effect of bismuth oxide on the optical features and gamma shielding efficiency of lithium zinc borate glasses. Ceramics International 2020;46(14):22883–8. https://doi.org/10.1016/j.ceramint.2020.06.061.

[26] Naseer KA, Marimuthu K, Al-Buriahi MS, Alalawi A, Tekin HO. Influence of Bi2O3 concentration on barium-telluro-borate glasses: Physical, structural and radiation-shielding properties. Ceramics International 2021;47(1):329–40. https://doi.org/10.1016/j.ceramint.2020.08.138.

[27] K.S. Coomaraswamy, P.J. Lumley, M.P. Hofmann, Effect of bismuth oxide radioopacifier content on the material properties of an endodontic Portland cement-based (MTA-like) system, J. Endod. 33 (2007) 295–298. https://doi.org/10.1016/j.joen.2006.11.018.

[28] J.M. Guerreiro-Tanomaru, A.L.G. Cornélio, C. Andolfatto, L.P. Salles, M. Tanomaru-Filho, pH and Antimicrobial Activity of Portland Cement Associated with Different Radiopacifying Agents, ISRN Dent. 2012 (2012) 469019. https://doi.org/10.5402/2012/469019.

[29] R. Grazziotin-Soares, M.H. Nekoofar, T.E. Davies, A. Bafail, E. Alhaddar, R. Hübler, A.L.S. Busato, P.M.H. Dummer, Effect of bismuth oxide on white mineral trioxide aggregate: chemical characterization and physical properties, Int. Endod. J. 47 (2014) 520–533. https://doi.org/10.1111/iej.12181.

[30] S. Azimkhani, A. Kalhor, A. Rahmani, A. Sohrabi, Investigation of Gamma-Ray Shielding and Strength Properties of Concrete Containing Bismuth and Barite, Iran J Sci Technol Trans Sci 43 (2019) 1967–1972. https://doi.org/10.1007/s40995-018-0655-0.

[31] I.M. Nikbin, M. Shad, G.A. Jafarzadeh, S. Dezhampanah, An experimental investigation on combined effects of nano-WO3 and nano-Bi2O3 on the radiation shielding properties of magnetite concretes, Progress in Nuclear Energy 117 (2019) 103103. https://doi.org/10.1016/j.pnucene.2019.103103.

[32] I.M. Nikbin, A. Rafiee, S. Dezhampanah, S. Mehdipour, R. Mohebbi, H.H. Moghadam, A. Sadrmomtazi, Effect of high temperature on the radiation shielding properties of cementitious composites containing nano- Bi2O3, Journal of Materials Research and Technology 9 (2020) 11135–11153. https://doi.org/10.1016/j.jmrt.2020.08.018.

[33] Y. Yao, X. Zhang, M. Li, R. Yang, T. Jiang, J. Lv, Investigation of gamma ray shielding efficiency and mechanical performances of concrete shields containing bismuth oxide as an environmentally friendly additive, Radiation Physics and Chemistry 127 (2016) 188–193. https://doi.org/10.1016/j.radphyschem.2016.06.028.

[34] H.O. Tekin, M.I. Sayyed, S.A.M. Issa, Gamma radiation shielding properties of the hematite-serpentine concrete blended with WO3 and Bi2O3 micro and nano particles using MCNPX code, Radiation Physics and Chemistry 150 (2018) 95–100. https://doi.org/10.1016/j.radphyschem.2018.05.002.

[35] K. Verdipoor, A. Alemi, A. Mesbahi, Photon mass attenuation coefficients of a silicon resin loaded with WO3, PbO, and Bi2O3 Micro and Nano-particles for radiation shielding, Radiation Physics and Chemistry 147 (2018) 85–90. https://doi.org/10.1016/j.radphyschem.2018.02.017.

[36] N.Z. Noor Azman, S.A. Siddiqui, R. Hart, I.M. Low, Effect of particle size, filler loadings and x-ray tube voltage on the transmitted x-ray transmission in tungsten oxide-epoxy composites, Appl. Radiat. Isot. 71 (2013) 62–67. https://doi.org/10.1016/j.apradiso.2012.09.012.

[37] R. Künzel, E. Okuno, Effects of the particle sizes and concentrations on the X-ray absorption by CuO compounds, Appl. Radiat. Isot. 70 (2012) 781–784. https://doi.org/10.1016/j.apradiso.2011.12.040.

[38] M.Z. Botelho, R. Künzel, E. Okuno, R.S. Levenhagen, T. Basegio, C.P. Bergmann, X-ray transmission through nanostructured and microstructured CuO materials, Appl. Radiat. Isot. 69 (2011) 527–530. https://doi.org/10.1016/j.apradiso.2010.11.002.

[39] N.Z.N. Azman, S.A. Siddiqui, I.M. Low, Characterisation of micro-sized and nano-sized tungsten oxide-epoxy composites for radiation shielding of diagnostic X-rays, Mater. Sci. Eng. C Mater. Biol. Appl. 33 (2013) 4952–4957. https://doi.org/10.1016/j.msec.2013.08.023.

[40] A. Aghaz, R. Faghihi, S.M.J. Mortazavi, A. Haghparast, S. Mehdizadeh, S. Sina, Radiation attenuation properties of shields containing micro and Nano WO3 in diagnostic X-ray energy range, IJRR 14 (2016) 127–131. https://doi.org/10.18869/acad-pub.ijrr.14.2.127.

[41] N. Asari Shik, L. Gholamzadeh, X-ray shielding performance of the EPVC composites with micro- or nanoparticles of WO3, PbO or Bi2O3, Appl. Radiat. Isot. 139 (2018) 61–65. https://doi.org/10.1016/j.apradiso.2018.03.025.

[42] P.V. Krivenko, M. Sanytsky, T. Kropyvnytska, The Effect of Nanosilica on the Early Strength of Alkali-Activated Portland Composite Cements, SSP 296 (2019) 21–26. https://doi.org/10.4028/www.scientific.net/SSP.296.21.

[43] M. Sanytsky, U. Marushchak, Y. Olevych, Y. Novytskyi, Nano-modified Ultra-rapid Hardening Portland Cement Compositions for High Strength Concretes, in: Z. Blikharskyy, P. Koszelnik, P. Mesaros (Eds.), Proceedings of CEE 2019, Springer International Publishing, Cham, 2020, pp. 392–399.

[44] Jones W, Gibb A, Goodier C, Bust P, Song M, Jin J (2019) Nanomaterials in construction – what is being used, and where? Constr Mater 172 (2): 49-62. doi:10.1680/jcoma.16.00011

[45] Ivanov LA, Xu LD, Bokova ES, Ishkov AD, Muminova SR (2020) R. Nanotechnologies: are view of inventions and utility models. Part V. Nano Constr. 12(6), 331–33. doi:10.15828/2075-8545-2020-12-6-331-338

[46] H. Aviv, S. Bartling, I. Grinberg, S. Margel, Synthesis and characterization of Bi2O3/HSA core-shell nanoparticles for X-ray imaging applications, J. Biomed. Mater. Res. B Appl. Biomater. 101 (2013) 131–138. https://doi.org/10.1002/jbm.b.32826.

[47] X. Zhu, Z. Lu, X. Liu, M. Song, G. Zhou, Z. Yu, L. Xu, Q. Liu, S. Han, J. Chu, Continuous microwave synthesis of Bi2O3 rods coated with a temperature-sensitive polymer, J Mater Sci 55 (2020) 11213–11225. https://doi.org/10.1007/s10853-020-04799-w.

[48] O. Gurler, U. Akar Tarim, Determination of Radiation Shielding Properties of Some Polymer and Plastic Materials against Gamma-Rays, Acta Phys. Pol. A 130 (2016) 236–238. https://doi.org/10.12693/APhysPolA.130.236.

[49] L. Gerward, N. Guilbert, K.B. Jensen, H. Levring, WinXCom—a program for calculating X-ray attenuation coefficients, Radiation Physics and Chemistry 71 (2004) 653–654. https://doi.org/10.1016/j.radphyschem.2004.04.040.

[50] D.C. Creagh, J.H. Hubbell, Problems associated with the measurement of X-ray attenuation coefficients. I. Silicon. Report of the International Union of Crystallography X-ray Attenuation Project, Acta Crystallogr A Found Crystallogr 43 (1987) 102–112. https://doi.org/10.1107/s0108767387099793.

[51] M.M. Sadawy, R.M. El Shazly, Nuclear radiation shielding effectiveness and corrosion behavior of some steel alloys for nuclear reactor systems, Defence Technology 15 (2019) 621–628. https://doi.org/10.1016/j.dt.2019.04.001.

[52] A.M. El-Khayatt, İ. Akkurt, Photon interaction, energy absorption and neutron removal cross section of concrete including marble, Annals of Nuclear Energy 60 (2013) 8–14. https://doi.org/10.1016/j.anucene.2013.04.021.

[53] P. Sikora, M. Abd Elrahman, D. Stephan, The Influence of Nanomaterials on the Thermal Resistance of Cement-Based Composites-A Review, Nanomaterials (Basel) 8 (2018). https://doi.org/10.3390/nano8070465.

[54] Q. Li, N.J. Coleman, Impact of Bi2O3 and ZrO2 Radiopacifiers on the Early Hydration and C-S-H Gel Structure of White Portland Cement, J. Funct. Biomater. 10 (2019). https://doi.org/10.3390/jfb10040046.

[55] Q. Li, N.J. Coleman, Early hydration of white Portland cement in the presence of bismuth oxide, Advances in Applied Ceramics 112 (2013) 207–212. https://doi.org/10.1179/1743676112Y.0000000058.

[56] R. Kumar, B. Bhattacharjee, Porosity, pore size distribution and in situ strength of concrete, Cement and Concrete Research 33 (2003) 155–164. https://doi.org/10.1016/S0008-8846(02)00942-0.

[57] Odler, M. Rößler, Investigations on the relationship between porosity, structure and strength of hydrated Portland cement pastes. II. Effect of pore structure and of degree of hydration, Cement and Concrete Research 15 (1985) 401–410. https://doi.org/10.1016/0008-8846(85)90113-9.

[58] S. Manninen, S. Koikkalainen, Determination of the effective atomic number using elastic and inelastic scattering of γ-rays, The International Journal of Applied Radiation and Isotopes 35 (1984) 965–968. https://doi.org/10.1016/0020-708X(84)90212-6.

[59] W.V. Mayneord, The significance of the röntgen, Acta Int. Union Against Cancer 2 (1937).

[60] R.C. Murty, Effective Atomic Numbers of Heterogeneous Materials, Nature 207 (1965) 398–399. https://doi.org/10.1038/207398a0.

[61] Zayed, A.m., M.a. Masoud, Alaa M. Rashad, A.m. El-Khayatt, K. Sakr, W.a. Kansouh, and M.g. Shahien. "Influence of Heavyweight Aggregates on the Physico-mechanical and Radiation Attenuation Properties of Serpentine-based Concrete." Construction and Building Materials 260 (2020): 120473. doi:10.1016/j.conbuildmat.2020.120473.

[62] B. Hołyńska, Study of the effect of grain size heterogeneity in the X-ray absorption analysis of simulated aqueous slurries, Spectrochimica Acta Part B: Atomic Spectroscopy 27 (1972) 237–245. https://doi.org/10.1016/0584-8547(72)80025-9.

[63] R. Florez, H.A. Colorado, A. Alajo, C.H.C. Giraldo, The material characterization and gamma attenuation properties of Portland cement-Fe3O4 composites for potential dry cask applications, Progress in Nuclear Energy 111 (2019) 65–73. https://doi.org/10.1016/j.pnucene.2018.10.022.

[64] A.M. El-Khayatt, NXcom – A program for calculating attenuation coefficients of fast neutrons and gamma-rays, Annals of Nuclear Energy 38 (2011) 128–132. https://doi.org/10.1016/j.anucene.2010.08.003.

Figure Captions:

Figure 1. SEM micrographs of Bi_2O_3 microparticles (left) and Bi_2O_3 nanoparticles (right).

Figure 2. TG curves of Bi_2O_3 micro- and nanoparticles.

Figure 3. Particle size distribution (PSD) of dry powders used for cement paste production.

Figure 4. Gamma-ray attenuation measurement experimental setup.

Figure 5. Schematic diagram of the experimental setup for neutron detection

Figure 6. Variation of $ln(I_o/I)$ versus thickness for BNP15 paste sample, irradiated with 0.911 MeV gamma-ray beam (left). Variation of ln (ϕ_0/ϕ) versus thickness for BMP15 paste sample, irradiated with slow neutron beam (right).

Figure 7. Consistency of cement pastes determined with the flow table method.

Figure 8. Compressive strength of cement pastes at 7 d (left) and 28 d (right)

Figure 9. Cumulative pore volume of cement pastes

Figure 10. Experimental and theoretical mass attenuation coefficients of cement pastes: (A) CP, (B) BNP5, (C) BNP10, (D) BNP15, (E) BNP20, and (F) BNP30 as a function of photon energy.

Figure 11. Experimental and theoretical mass attenuation coefficients of BMPs: (A) BMP5, (B) BMP10, (C) BMP15 and (D) BMP20 as a function of photon energy.

Figure 12. Experimental mass attenuation coefficients for (A) CP and BNP20 and (B) CP and BMP20, as a function of photon energy.

Figure 13. The linear attenuation coefficient of Bi_2O_3 nanoparticle cement paste as a function of weight percentage of Bi_2O_3, over two energy regions: (A) (0.08-0.238 MeV) and (B) (0.911-2.614 MeV).

Table captions:

Table 1. Chemical compositions of Portland cement [wt.-%]

Table 2. Cement paste mix design

Table 3. Basic parameters of pore structure measured by MIP and water accessible porosity

Table 4. Mean atomic number, mean atomic mass, single-value of Z_{eff} calculated with different empirical expressions, maximum and minimum values of $Z_{PI,eff}$ and $Z_{PE,eff}$ are given for different Bi_2O_3 nanoparticles pastes; similar values were obtained for the microparticle cement samples.

Table 5. Experimental linear attenuation coefficients μ (cm^{-1}) of γ-rays of cement pastes having Bi$_2$O$_3$ micro- and nanoparticles; experimental error $\leq$ 5%.

Table 6. Experimental HVL (in cm) of γ-rays for Bi$_2$O$_3$ micro and nanoparticles cement pastes; with experimental errors $\leq$ 4%.

Table 7. Experimental macroscopic cross-sections of slow neutron Σ_{Slow} and the calculated removal cross-section of fast neutron Σ_R for micro-and nanoparticles cement pastes. The corresponding HVLs are listed.

Comparison of the effects of bismuth oxide (Bi₂O₃) micro-and nanoparticles on the mechanical, microstructural, and γ-ray / neutron shielding properties of Portland cement pastes

Pawel Sikora[1,2,*], Ahmed M. El-Khayatt[3,4], H.A. Saudi[5], Sang-Yeop Chung[6], Dietmar Stephan[1], Mohamed Abd Elrahman[7,†]

[1] Building Materials and Construction Chemistry, Technische Universität Berlin, Germany
[2] Faculty of Civil and Environmental, West Pomeranian University of Technology Szczecin, Szczecin
[3] Department of Physics, College of Science, Imam Mohammad Ibn Saud Islamic University, (IMSIU), Riyadh, Saudi Arabia
[4] Reactor Physics Department, Nuclear Research Centre, Atomic Energy Authority, 13759, Cairo, Egypt
[5] Department of Physics, Faculty of Science, Al-Azhar University, Women Branch, Nasr City, Cairo, Egypt
[6] Department of Civil and Environmental Engineering, Sejong University, Seoul 05006, Republic of Korea
[7] Structural Engineering Department, Mansoura University, Mansoura City 35516, Egypt

SUPPLEMENTARY MATERIAL

Corresponding authors: (1) Pawel Sikora – email: pawel.sikora@zut.edu.pl; Building Materials and Construction Chemistry, Technische Universität Berlin, Germany and (2) Mohamed Abd Elrahman – email: mohamedattia@mans.edu.eg; Structural Engineering Department, Mansoura University, Mansoura City 35516, Egypt.

Table S1. Elemental weight fraction (w %) and the elemental density (ρ_i) as it appears in the paste sample.

| Elem.	CP		Bi$_2$O$_3$ 5 %			Bi$_2$O$_3$ 10 %			Bi$_2$O$_3$ 15 %			Bi$_2$O$_3$ 20 %			Bi$_2$O$_3$ 30 %	
				ρ_i			ρ_i			ρ_i			ρ_i			
	w %	ρ_i	w %			w %			w %			w %			w %	ρ_i
				BMP	BNP		BMP	BNP		BMP	BNP		BMP	BNP		
H	3.20	0.101	3.08	0.113	0.115	2.96	0.117	0.119	2.84	0.120	0.121	2.71	0.122	0.124	2.45	0.117
C	0.26	0.008	0.25	0.009	0.009	0.24	0.010	0.010	0.23	0.010	0.010	0.22	0.010	0.010	0.20	0.010
O	50.76	1.599	49.29	1.814	1.839	47.78	1.887	1.916	46.23	1.955	1.974	44.63	2.013	2.035	41.27	1.973
Na	0.11	0.004	0.11	0.004	0.004	0.10	0.004	0.004	0.10	0.004	0.004	0.09	0.004	0.004	0.09	0.004
Mg	0.91	0.029	0.88	0.032	0.033	0.84	0.033	0.034	0.81	0.034	0.034	0.77	0.035	0.035	0.70	0.033
Al	2.01	0.063	1.94	0.071	0.072	1.87	0.074	0.075	1.79	0.076	0.076	1.71	0.077	0.078	1.54	0.074
Si	6.85	0.216	6.61	0.243	0.246	6.35	0.251	0.255	6.09	0.257	0.260	5.82	0.262	0.265	5.25	0.251
S	1.62	0.051	1.56	0.057	0.058	1.50	0.059	0.060	1.43	0.061	0.061	1.37	0.062	0.063	1.24	0.059
K	0.43	0.013	0.41	0.015	0.015	0.40	0.016	0.016	0.38	0.016	0.016	0.36	0.016	0.017	0.33	0.016
Ca	32.67	1.029	31.49	1.159	1.175	30.27	1.196	1.214	29.02	1.227	1.239	27.72	1.250	1.264	25.02	1.196
Fe	1.18	0.037	1.14	0.042	0.042	1.09	0.043	0.044	1.05	0.044	0.045	1.00	0.045	0.046	0.90	0.043
Bi	-	-	3.25	0.120	0.121	6.60	0.261	0.264	10.04	0.425	0.429	13.59	0.613	0.620	21.02	1.005
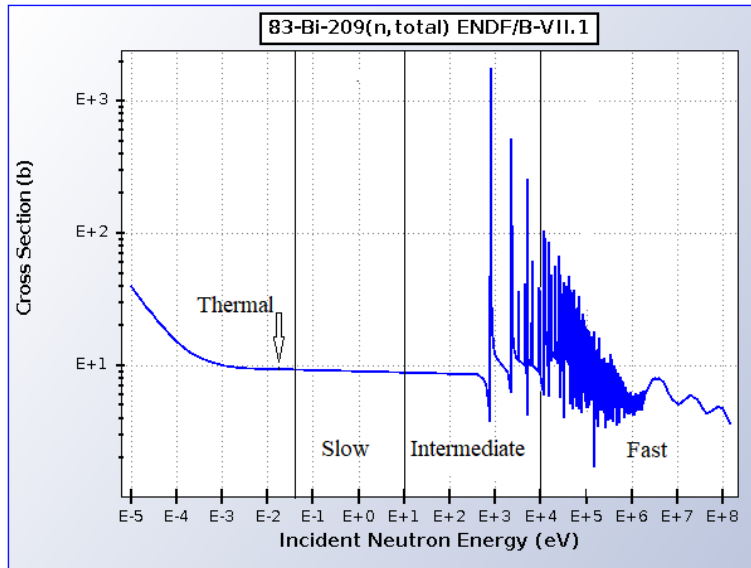
Figure S1. Energy dependent of total neutron cross section of Bi-209 nucleus, relatively small values are noticed for Σ_{Slow}. Based on [1].
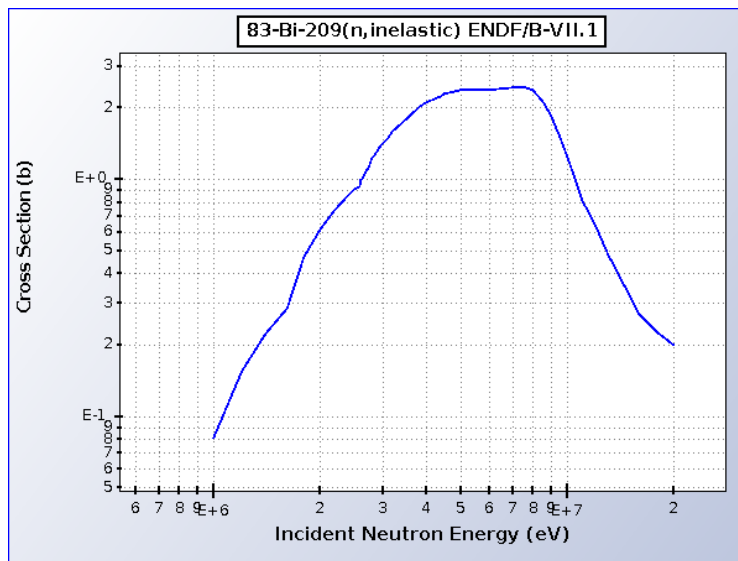

Figure S2. Energy dependent of the inelastic neutron scattering cross section of Bi-209 nucleus, the maximum values are recorded in the energy region 4 - 9 MeV. Based on [1].

References:

[1] Pritychenko B., Sonzogni AA. (2008) Sigma: Web Retrieval Interface for Nuclear Reaction Data. Nuclear Data Sheets 109 (12) 2822-2827. https://doi.org/10.1016/j.nds.2008.11.017